

A superconducting full-wave bridge rectifier

Matteo Castellani, Owen Medeiros, Alessandro Buzzi, Reed A. Foster, Marco Colangelo, and Karl K. Berggren*

Dept. of Electrical Engineering and Computer Science, Massachusetts Institute of Technology, Cambridge, MA, USA

E-mail: mcaste@mit.edu

Abstract

Superconducting thin-film electronics are attractive for their low power consumption, fast operating speeds, and ease of interface with cryogenic systems such as single-photon detector arrays, and quantum computing devices. However, the lack of a reliable superconducting two-terminal asymmetric device, analogous to a semiconducting diode, limits the development of power-handling circuits, fundamental for scaling up these technologies. Existing efforts to date have been limited to single-diode proofs of principle and lacked integration of multiple controllable and reproducible devices to form complex circuits. Here, we demonstrate a robust superconducting diode with tunable polarity using the asymmetric Bean-Livingston surface barrier in niobium nitride micro-bridges, achieving a 43% rectification efficiency. We then realize and integrate several such diodes into a bridge rectifier circuit on a single microchip that performs continuous full-wave rectification up to 3 MHz and AC-to-DC conversion in burst mode at 50 MHz with an estimated peak power efficiency of 60%.

Superconducting nanowire single-photon detectors (SNSPD) arrays are expected to be of key importance to the future development of photonic quantum computing,¹ quantum communication,² optoelectronic spiking neural networks,³ and high-energy physics.⁴ Scaling

up these systems requires the integration of cryogenic co-processors for readout and signal processing,⁵⁻¹⁰ and interconnection between many modular units as in superconducting quantum computing platforms.^{11,12} Therefore, it is crucial to build architectures capable of delivering and handling significant power at cryogenic stages, while dynamically tuning bias levels, minimizing cross-talk and electrical noise, and maintaining thermal isolation. Any solution to this problem will have to leverage the intrinsic energy efficiency of thin-film superconductors, be compatible with standard materials used for superconducting detectors and electronics, and interface with conventional circuitry.

In modern integrated circuits, diodes are fundamental components for power control and distribution. As such, superconducting diodes will be needed for efficient and compact bias-handling systems needed in cryogenic electronics and detectors. The main functionality enabled by superconducting diodes would be AC-to-DC conversion at low temperatures (e.g. using full-wave bridge rectifiers) to provide stable and tunable DC bias currents through RF signals. Such an operation might be useful to deliver power from room temperature using a limited number of RF lines or to interconnect different sub-systems of the same cryogenic architecture. Other typical functionalities of semiconducting diodes could be realized with superconductors, such as frequency mixing, signal modulation, voltage-controlled oscillation, and isolation; benefiting the development of several cryogenic platforms.

The superconducting diode effect (SDE) manifests in asymmetric critical currents for opposite current directions in a superconducting device. This phenomenon has been recently demonstrated using multiple technologies¹³ that primarily rely on the combined effect of a magnetic field and spin-orbit coupling^{14,15} or the Josephson effect.¹⁶⁻¹⁸ Moreover, field-free superconducting diodes have also been realized.^{19,20}

Despite impressive technical progress in the formation of individual devices, and the recent demonstration of half-wave rectification at 100 kHz,²¹ diode effects have not been explored for near-term use in complex and useful circuits that require more than a single diode. Past diode demonstrations had limitations such as: low rectification efficiency (η), the need

for Tesla-scale applied magnetic field, or the use of complex geometries and heterostructures requiring materials processing that is incompatible with conventional superconducting circuits. Thus, the assumption that cryogenic circuits could one day usefully take advantage of these SDEs remains to be proven.

Among the variety of proposed SDEs, the vortex diode effect, based on the asymmetric Bean-Livingston surface barrier²² in micro-bridges, has a great potential for realizing diode-based circuits at a large scale because: it requires the patterning of only a single layer; it operates with milliTesla-scale fields; it can generate a high-resistance state (useful to interface with traditional electronics) and; it can be implemented in essentially any superconductor. In particular, implementing vortex diodes in niobium nitride thin films opens the door to a wide range of applications considering that such material has been widely used for high-performance SNSPDs,²³ nanocryotron digital circuits that can be monolithically integrated with SNSPDs,^{6,7,24-27} microwave devices,^{28,29} spiking neural networks,^{30,31} and comparators that interface Josephson junctions with conventional electronics.³²

The vortex diode effect was initially proposed by Vodolazov et al.,³³ and then observed by Cerbu et al.³⁴ in aluminum wires with controlled edge defects, and by Semenov et al. in NbN SNSPDs with 90° turns.³⁵ However, the first diode based on this SDE was only recently demonstrated by Hou et al.³⁶ and used controlled edge defects on straight vanadium micro-bridges under an applied out-of-plane field of a few milliTesla. In this device, the efficiency was also boosted from 50% to 65% by introducing an adjacent thin layer of a ferromagnetic material, which eliminated the need for geometrical defects and external fields. The vortex diode effect has been recently demonstrated also using NbTiN nanowires³⁷ ($\eta = 24\%$), and NbN micro-bridges ($\eta = 30\%$);³⁸ however, the NbN-based devices relied on random edge defects introduced during the fabrication process, thus limiting the device reproducibility. Overcoming this limitation would help realize a reliable and reproducible NbN diode useful to design AC-to-DC converters in power distribution architectures.

In this work, we demonstrate the potential of using vortex diodes for designing power-

handling systems by combining them into a non-trivial circuit: a full-wave bridge rectifier composed of four integrated operational diodes. With this circuit, we demonstrated sustained full-wave rectification of sinusoidal signals at 3 MHz; rectification of a continuous pulsing waveform at 20 MHz; and AC-to-DC conversion at 50 MHz for limited time intervals. We implemented the vortex diodes using micro-bridges with controlled triangular edge defects, following Hou et al.³⁶ but using NbN as the superconducting material. We characterized both stand-alone diodes and bridge rectifiers by studying how the rectification efficiency and input current margins change as a function of the field, frequency, and shape of the signal. We also created an LTspice model of the diode to estimate the power efficiency of the AC-to-DC conversion and facilitate the design of larger diode-based circuits. To show the prospect of using such devices in circuits at a larger scale, we designed and simulated an architecture, based on the demonstrated AC-to-DC converter, to bias a network of 10 SNSPDs with dynamically tunable DC currents, by frequency multiplexing the bias levels on a single RF line as described in the supplementary material.

Bridge rectifier with vortex diodes

Our vortex diodes were 1 μm wide wires patterned on NbN films with three different thicknesses (9 nm, 13 nm, and 14 nm), deposited on a 300 nm thick thermal-silicon-oxide (SiO_2) on silicon substrate. Figure 1a shows the scanning electron micrograph of the device and an illustration of the operating principle. The triangular notch lowers the vortex surface barrier on the left side due to current crowding,³⁹ while the barrier on the right edge remains unchanged. A current I^+ generates a Lorentz force that pushes vortices towards the center of the wire. When this force is large enough, vortices cross the wire from the lower barrier on the left, generating a hotspot (resistive state). When an out-of-plane magnetic field is applied, a screening current circulates at the edges of the wire (Meissner effect). Since this Meissner current flows in opposite directions on the two edges, the surface barrier of one edge

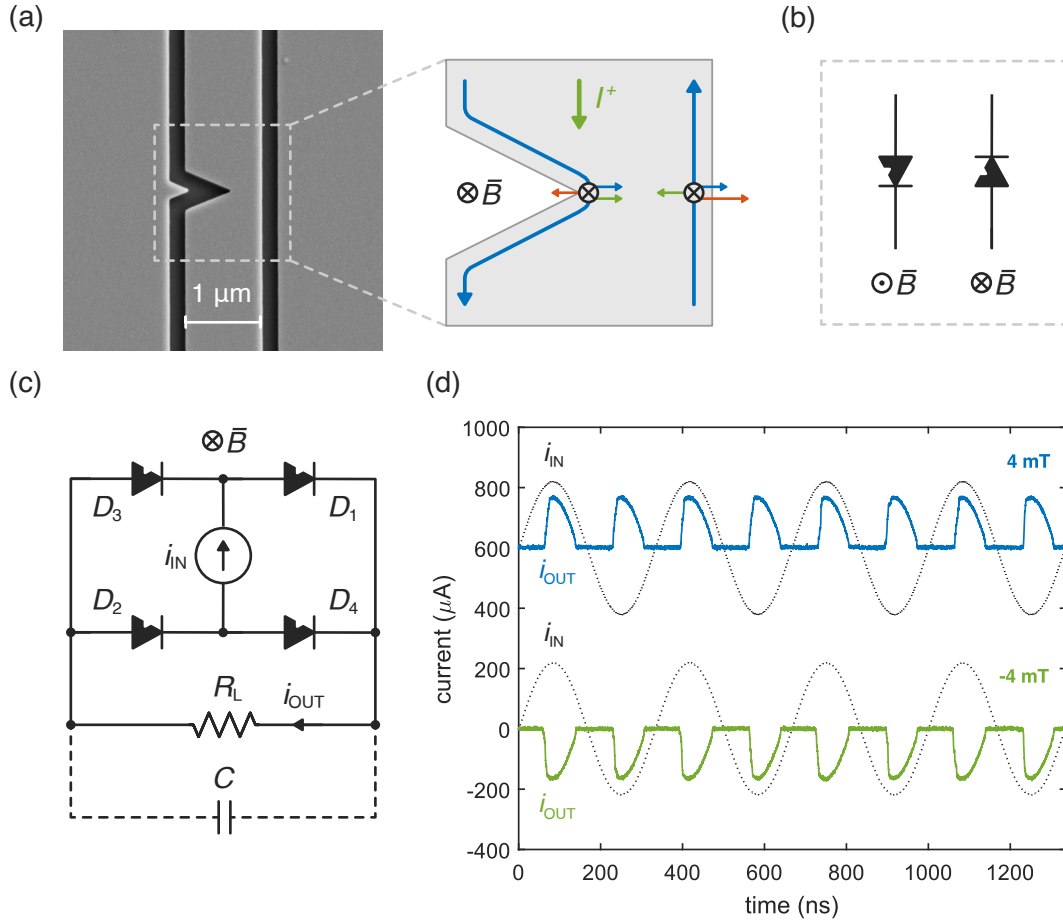


Figure 1: Superconducting diode and bridge rectifier. (a) Scanning electron micrograph of a superconducting diode, fabricated on a 14 nm thick film of niobium nitride. The constriction is 400 nm wide and the notch has an angle of 45° . The gray regions are niobium nitride, and the dark borders of the traces show the underlying SiO_2 substrate. The ground plane surrounds all the traces. The right inset depicts the working principle of a vortex diode when an entering out-of-plane magnetic field is applied, and a current I^+ passes through the device. Vortex dynamics are governed by three forces: force due to circulating current formed by the Meissner effect (horizontal blue arrows); Lorentz force due to I^+ (horizontal green arrows) and; force due to the surface barriers (red arrows). The net force pushes vortices from left to right. (b) Circuit symbols for superconducting diodes with positive or negative applied field. The field is entering the plane and the notch is on the left edge of the device. Inverting the field orientation changes the polarity of the diode. (c) Circuit schematic of the superconducting bridge rectifier driving a resistive load R_L . A smoothing capacitor C (dashed line) can be added in parallel to R_L to obtain a DC output current for AC-to-DC conversion. (d) Experimental full-wave current rectification of a 3 MHz sinusoidal signal i_{IN} (black dashed traces), with $R_L = 50 \Omega$ and without smoothing capacitor, and for both positive (blue trace) and negative (green trace) applied field. Traces are vertically shifted for clarity. Each trace is the average of 10 different traces acquired in sequence, to increase the signal-to-noise-ratio (one of the 10 traces is shown in the supplementary material).

is lowered, while the other is increased. Inverting the field direction inverts the direction of the circulating current, and thus reverses the surface barrier suppression, inducing the diode effect with opposite polarity. Figure 1b shows the associated circuit symbols.

We optimized the diode by patterning 18 superconducting devices on a 14 nm thick film with constant wire width (1 μm) but varying constriction width and aperture angle of the triangular defect. We observed a SDE in every device at 4.2 K, with consistent diode polarity and a similar rectification efficiency (η). The maximum value of η was obtained using a notch with a 45° angle, and a 400 nm wide constriction (figure 1a).

Bridge rectifiers are more power efficient than single-diode rectifiers in AC-to-DC current conversion because both halves of the input waveform are rectified (full-wave rectification). Therefore, such circuits are preferable for power distribution networks. After rectification, the DC current is usually achieved by using a low-pass filter. Figure 1c shows the circuit schematic of the superconducting bridge rectifier driven by an ideal current source and coupled to the low-pass filter. Thanks to the duality between superconducting diodes and their conventional counterparts, the topology of the circuit is familiar. The rectifier is composed of four vortex diodes (D_1 , D_2 , D_3 , and D_4) connected in a superconducting loop.

Firstly, we tested just the bridge circuit with a surface-mount resistor as a load, obtaining full-wave rectification of various input waveforms while using differential inputs and outputs to achieve isolation from the ground. We then added a smoothing capacitor to the output to demonstrate AC-to-DC conversion. Figure 1d shows full-wave rectification of a 3 MHz sinusoidal signal (without smoothing capacitor), for two values of the applied magnetic field. The output current could be tuned by flipping the field, as all the diodes in the circuit had tunable polarity.

Rectification efficiency

The rectification efficiency $\eta = \frac{|I_c^+| - |I_c^-|}{|I_c^+| + |I_c^-|}$ is a critical figure of merit to be maximized for optimal rectification. We measured the I-V characteristic of the diodes to extract the positive and negative critical currents (I_c^+ and I_c^- respectively). Figure 2a shows the I-V curves of a diode patterned on the 14 nm thick film, for different values of the field. With positive magnetic fields (entering the plane) the negative critical current $|I_c^-|$ increased, and the positive critical current $|I_c^+|$ decreased. Negative magnetic fields caused the opposite effect.

We studied how the critical currents and rectification efficiency vary with the magnetic field by applying a 1 kHz triangular wave to a device shunted with 1 M Ω . The upper panel of figure 2b shows that $|I_c^+|$ and $|I_c^-|$ were equal at zero magnetic field. $|I_c^-|$ linearly increased with an increasing positive field up to a peak value, while $|I_c^+|$ decreased. After the peak, $|I_c^-|$ linearly decreased because the surface barrier on the right edge became smaller than the barrier on the left. At about ± 5.5 mT, the relation ceased to be linear and both negative and positive currents approached similar low values because bulk vortex pinning effects dominated.³⁸ The peak of $|I_c^-|$ was higher than the peak of $|I_c^+|$, as observed by Suri et al.³⁸ The lower panel of figure 2b shows the rectification efficiency η as a function of the magnetic field for two different film thicknesses (14 nm and 9 nm). For the 14 nm thick device the maximum rectification efficiency of 35 % was reached at 3.3 mT. The 9 nm thick device had a maximum η of 36 % at 4 mT.

Demonstrating signal rectification at frequencies in the MHz range would enable radio-frequency signals to be processed and converted into DC levels, and would thus be enabling for the future development of this technology. Therefore, we studied how the rectification efficiency varies as a function of the frequency of an applied sinusoidal signal. Figure 2c shows the value of η at frequencies between 10 Hz and 5 MHz for three different film thicknesses (with a 50 Ω shunt). For all the thicknesses, η quickly dropped to zero at frequencies higher than 100 kHz (a similar cutoff has been observed by Chahid et al.²¹). In these measurements, the cutoff seemed to be independent of the thickness. Nevertheless, η increased with thinner

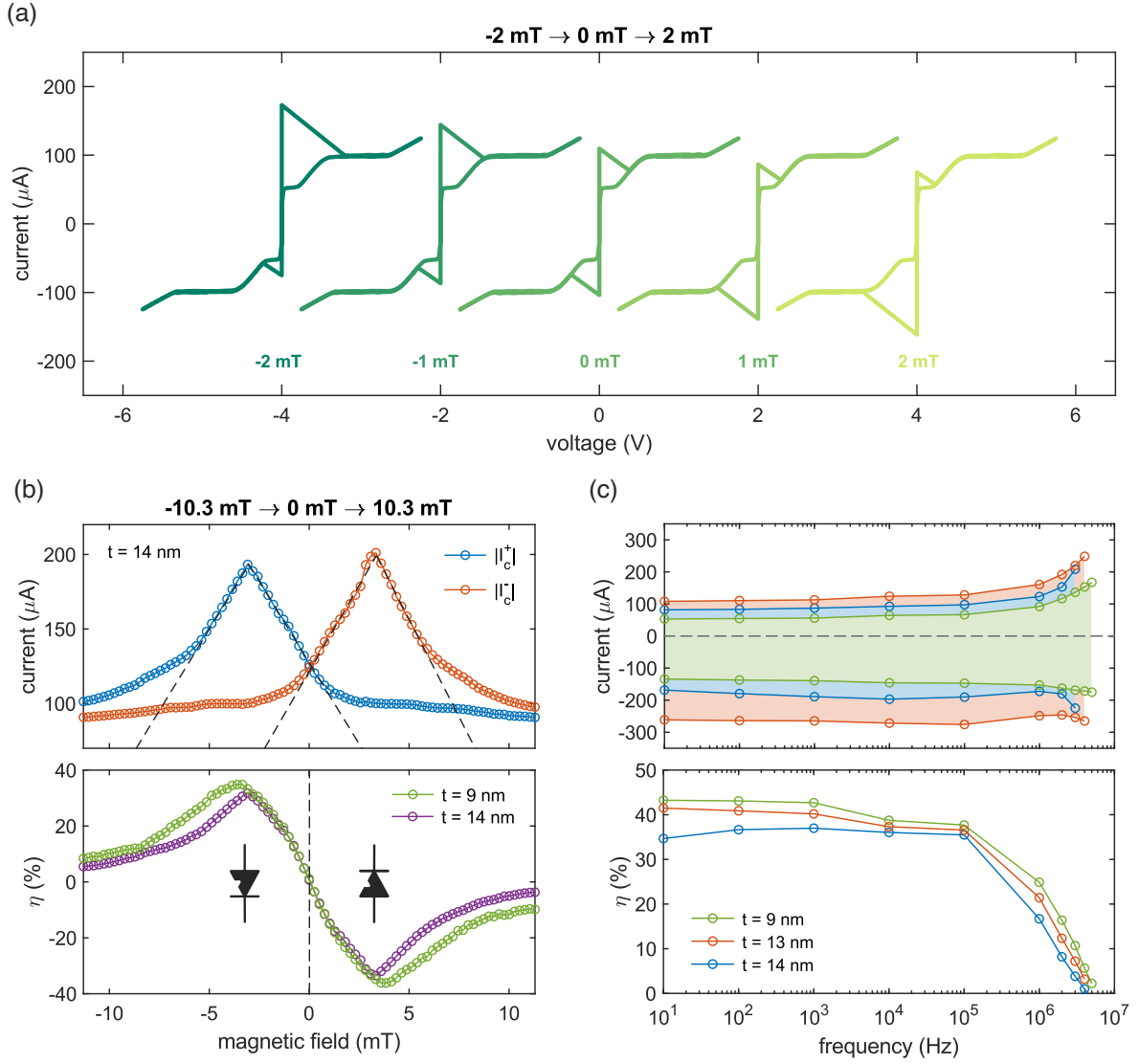


Figure 2: Characterization of superconducting diodes. (a) I-V curves of a superconducting diode, fabricated on a 14 nm thick film, for different values of magnetic field. The field was swept from -2 mT to 2 mT. The curves are shifted along the x-axis for clarity. (b) Upper panel: positive and negative critical currents ($|I_c^+|$ and $|I_c^-|$) as a function of the magnetic field (field swept from -10.3 mT to 10.3 mT.). Dashed lines fit the linear regions of the plot. Lower panel: Rectification efficiency η as a function of the magnetic field with a triangular wave as bias signal, for two different film thicknesses and the same geometry. (c) Current margins to maintain a superconducting state (upper panel), and rectification efficiency η (lower panel), for a sinusoidal bias signal at different frequencies. Devices with three different thicknesses $t = 9, 13, 14$ nm were tested. For each t , the applied magnetic field was chosen to maximize η at 10 Hz. In the top panel, the data points above and below zero correspond to $|I_c^-|$ and $|I_c^+|$ respectively. The colors of traces in both panels are associated with the legend.

films, as predicted by Vodolazov et al.³³ The highest rectification efficiency of 43% was achieved at 10 Hz, for the 9 nm thick film. At the same frequency (1 kHz) and same thickness (9 nm or 14 nm), we observed different maxima of η for sinusoidal signals with a 50 Ω shunt (figure 2c) and triangular waves with a 1 M Ω shunt (figure 2b). This result shows that shape of the signal and shunt impedance influence the efficiency.

Using a single vortex diode patterned on the 14 nm thick film, we then demonstrated half-wave rectification of a triangular waveform at 1 kHz, with a 1 M Ω load (see supplementary material).

Margins for full-wave rectification

Figure 3a shows a superconducting bridge rectifier patterned on a 13 nm thick film. The left branch of the loop is composed of D_2 and D_3 , the right branch is composed of D_1 and D_4 . Both branches had a characteristic total kinetic inductance (L_L and L_R respectively), and the ratio L_L/L_R influenced the operations and margins of the device. We fabricated bridge rectifiers with $L_L/L_R = 1$ and $L_L/L_R = 10$.

Figure 3b shows the I-V curves of two devices with different L_R/L_L , while the applied positive field (4 mT) was set to maximize η . For both devices, we observed two switching events at positive and negative currents: I_{c1}^+ , I_{c2}^+ , I_{c1}^- , and I_{c2}^- . For the positive quadrant of the plot, when the current through D_3 and D_4 was lower than their I_c^+ ($I_{IN} < I_{c1}^+$), the input current I_{IN} was split into the two branches. Thus, no hotspots were generated and no current was provided to the load resistor (zero voltage in the I-V curve). In this region, for $L_R/L_L = 1$, the current was equally split. For $L_L/L_R = 10$, most of the current flowed into the left branch. When the currents through D_3 and D_4 exceeded I_c^+ , D_3 and D_4 switched to the resistive state, and the input current was diverted to D_1 and D_2 , which remained in the superconducting state. Therefore, I_{IN} passed through the load resistor, and the slope in the I-V curve was $1/R_L$ ($I_{c1}^+ < I_{IN} < I_{c2}^+$). When the currents through D_1 and D_2 exceeded

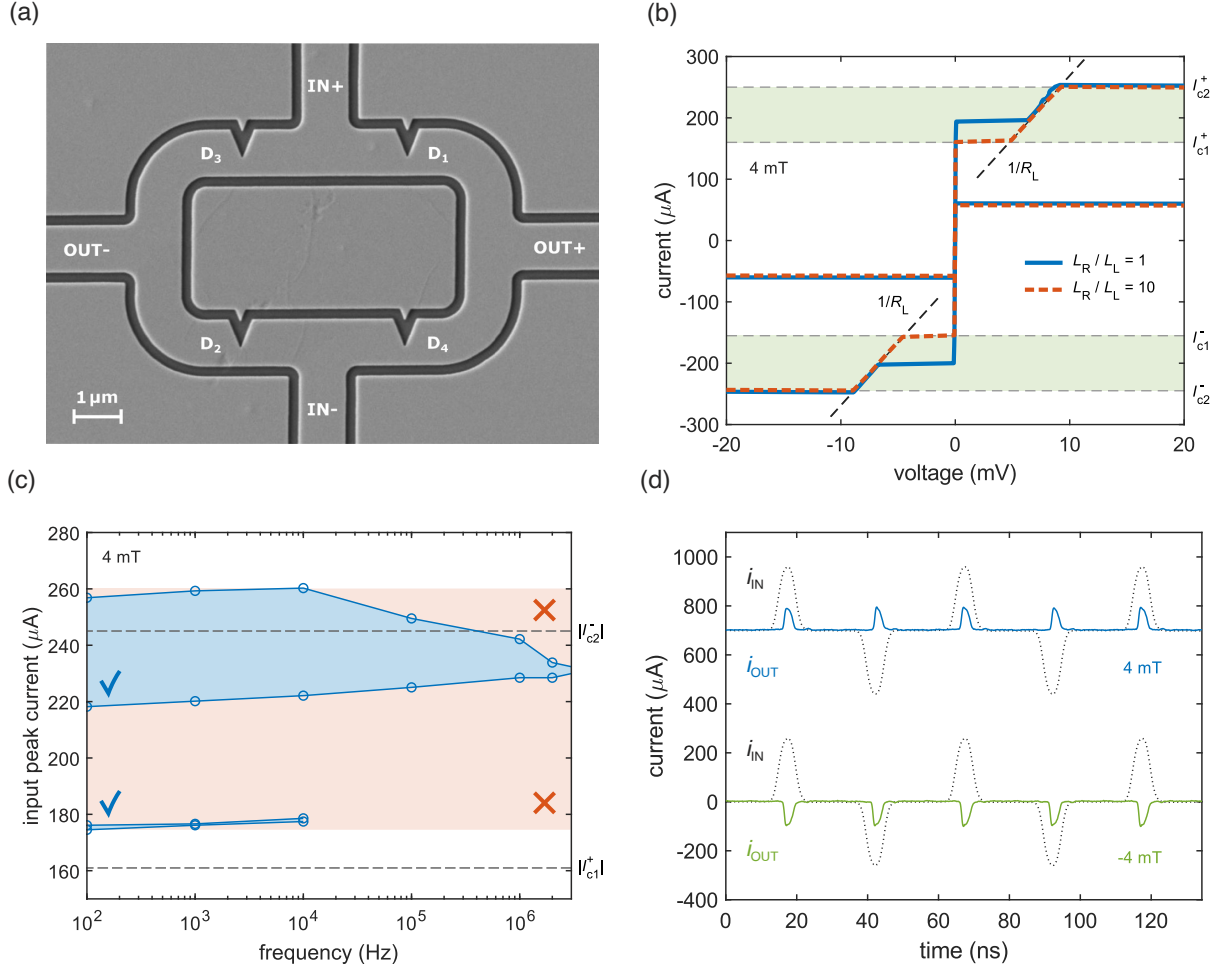


Figure 3: Characterization of superconducting bridge rectifiers. (a) Scanning electron micrograph of a superconducting bridge rectifier, fabricated on a 13 nm thick film of niobium nitride ($L_R/L_L = 1$). The gray regions are niobium nitride, and the dark borders of the traces show the underlying SiO_2 substrate. The ground plane surrounds all the traces. The current source connects the IN- port to the IN+ port. The load resistor R_L is connected between OUT- and OUT+ (see figure 1c). The geometry of the rectifier with $L_L/L_R = 10$ is shown in the supplementary material. (b) I-V curve of a bridge rectifier for two different values of L_R/L_L , with a 4 mT field ($R_L = 50 \Omega$). Green regions indicate ideal current margins for the correct operation of the rectifier with $L_R/L_L = 10$. (c) Margins to obtain correct full-wave rectification, for the input current amplitude of a periodic sinusoidal signal i_{IN} , as a function of frequency (field: 4 mT). The two dashed lines indicate the ideal minimum and maximum currents to operate the rectifier according to figure b ($L_R/L_L = 10$). In blue regions, the device correctly rectifies. In red and white regions, the device does not rectify. (d) Full-wave rectification of periodic current pulses at 20 MHz, for positive and negative magnetic fields. The measured input signals v_{IN} are shown with dashed lines. Traces are vertically shifted for clarity. Each trace is the average of 100 different traces acquired in sequence, to increase the signal-to-noise-ratio. An output pulse was observed for every semi-period.

I_c^- ($I_{IN} > I_{c2}^+$), all the diodes switched, resulting in a high resistance state in the I-V curve. When the input current was negative, D_3 and D_4 were superconducting and D_1 and D_2 were resistive so that the output current could flow in the same direction as with positive I_{IN} .

For ideal full-wave signal rectification, the device should operate with a positive peak input current between I_{c1}^+ and I_{c2}^+ , and a negative peak current between I_{c2}^- and I_{c1}^- in figure 3b. In theory, the switching currents, and thus the margin of the device, depend on the rectification efficiency and the geometry of the rectifier with the following relations: $|I_{c1}^+| = |I_{c1}^-| \approx (1 + L_L/L_R)|I_c^+|$ and $|I_{c2}^+| = |I_{c2}^-| \approx |I_c^-|$ (derived by applying a current division between the two branches of the loop). However, we observed a slight asymmetry in the positive and negative critical currents and a deviation from the ideal theory. For $L_R/L_L = 10$: $|I_{c1}^+|$ was 161 μA and $|I_{c1}^-|$ was 155 μA instead of 119 μA ; $|I_{c2}^+|$ was 251 μA and $|I_{c2}^-|$ was 245 μA instead of 261 μA . Nevertheless, the largest margins were obtained when the inductance ratio was highest, as expected. Therefore, we used the device with $L_R/L_L = 10$ for all the following analysis. Given the values of switching currents, the resulting margins for the current amplitude of an input signal to be rectified should have been between 161 μA and 245 μA but margins could also depend on the frequency and shape of the input signal.

We further characterized the rectifier to study how the margins varied as a function of the frequency of a sinusoidal signal. Figure 3c shows the range of i_{IN} amplitudes (the region in blue) that allowed full-wave rectification, for different input frequencies. Outside of these margins, either only half-wave rectification was observed, or the output current was zero. The red region is delimited by the minimum and maximum i_{IN} obtained where correct operation occurred somewhere in the measured spectrum. In theory, these values should have been $|I_{c1}^+|$ and $|I_{c2}^-|$ from figure 3b, but we observed a positive shift of about 15 μA for both of them, which could be caused by the use different measurement setups. Moreover, the margins were narrower than predicted from the I-V curve. In particular, they were discontinuous between 100 Hz and 10 kHz: for example, at 100 Hz, the device worked properly between 175 μA and 176 μA , it did not operate correctly from 176 μA to 218 μA , and it rectified again between

218 μA and 257 μA . Above 10 kHz the margins were continuous but gradually reduced from 38 μA at 10 kHz to 3 μA at 3 MHz. The observation of the 3 MHz frequency limit in both the diode and the bridge rectifier suggests that the speed constraint was fundamental to the hotspot dynamics of the diode, and most likely depends on the thermal behavior of the devices during hotspot growth and relaxation.

The ratio between the peak output current and input current amplitude varied with frequency. At 100 Hz, with a 240 μA amplitude, the ratio was 0.91, and it decreased to 0.76 at 3 MHz. From this result, we conclude that a small portion of input current always flowed through the two diodes in the resistive state instead of flowing into the load and that this current increased with the frequency. Most Likely, such current maintained their resistive state, and it was frequency-dependent because η decreased with the frequency (with a lower η , more current flowed into the diodes to obtain a switch).

Figure 3d shows that the circuit could also correctly rectify 10 ns wide pulses at a maximum frequency of 20 MHz, but with a lower efficiency than for a sinusoidal signal at 3 MHz: the peak output current was about 3 times smaller than the input peak current. The higher operating speed with pulses is consistent with the idea that the duty cycle of the waveform, and thus the heating of the substrate, is critical to correct operation.

We created a simple LTspice model of the vortex diode, based on the electrothermal model of NbN nanowires,⁴⁰ to better describe the experimental behaviors of the bridge rectifier. In simulations, we observed an effect that might explain the reduction of the margins (see supplementary material). However, we did not find a clear explanation for the discontinuous operation between 100 Hz and 10 kHz.

AC-to-DC conversion

The device could rectify continuous sinusoidal signals up to 3 MHz. However, we observed rectification at higher frequencies in burst mode. Figure 4a shows a fully rectified 50 MHz

sinusoidal signal applied for 100 ns with a 1 μ s burst period. At this frequency, a longer burst duration caused instability in the system (only a portion of semi-periods were rectified after 100 μ s). We believe the observed difference in maximum operating frequency between the continuous and burst modes was due to the system heating up significantly during the continuous operation, while having time to cool off between bursts in burst mode.

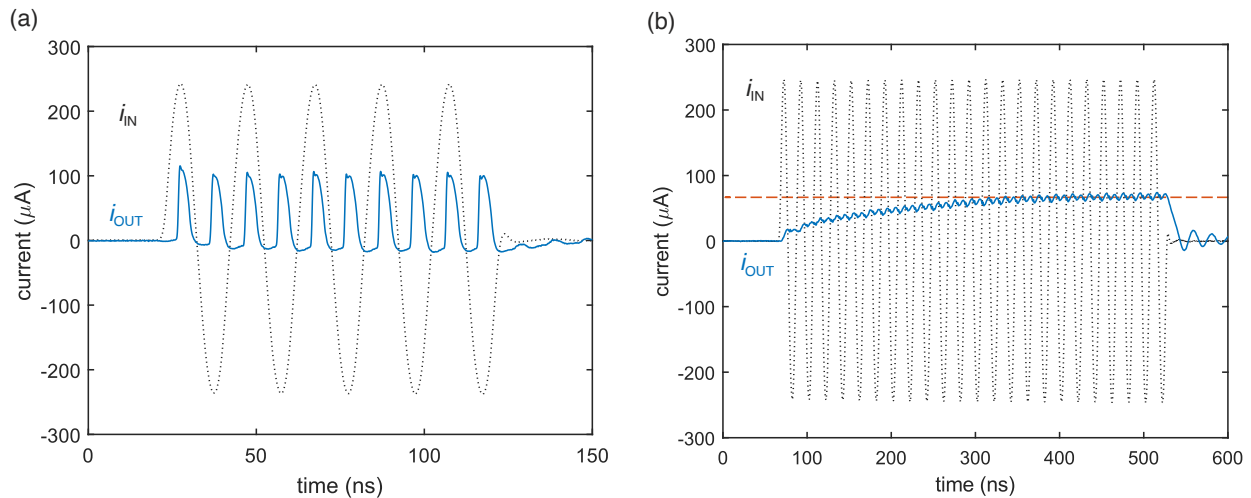


Figure 4: Operating the bridge rectifier and AC-to-DC converter at 50 MHz. (a) Full-wave rectification of a sinusoidal signal for 100 ns. The input signal i_{IN} is set to burst mode with a 1 μ s burst period. The load R_L is 50 Ω (100 Ω surface-mount resistor in parallel with the 100 Ω differential mode impedance from the amplifiers). There is a transient for the lower level of the output signal i_{OUT} because the input capacitance of the used amplifiers need to be charged. (b) AC-to-DC conversion with a 500 pF smoothing capacitor (see figure 1c), for 440 ns in burst mode (the burst period is 100 μ s). The red dashed line indicates the value of the output DC current (69 μ A) between 340 ns and 520 ns.

Considering that the circuit could operate up to 50 MHz in burst mode, we demonstrated AC-to-DC conversion by shunting the load R_L with a 500 pF surface-mount smoothing capacitor (dashed line in figure 1c). Figure 4b shows the output current of the converter through the load resistor. The device could operate for a 460 ns long burst (burst period: 100 μ s), with an 8% ripple whose amplitude was set by the capacitance. The DC value of the current saturated to 69 μ A. The waveform in the figure was averaged over 100 signals to increase the SNR and thus extract the ripple amplitude. A single trace without averaging is shown in the supplementary material. After a start-up time of about 300 ns, the capacitor

was correctly charged at each semi-period, for all the acquired signals.

It is worth mentioning that including the smoothing capacitor enabled correct rectification for a longer burst duration compared to the configuration with a resistive load. This difference likely comes from the intrinsic dependence on load impedance for the hotspot growth and, consequently, for thermal dissipation.

We could not experimentally extract the power efficiency of the circuit because sensing the input voltage would have altered the operation of the device. Therefore, we estimated the efficiency by mimicking the AC-to-DC conversion with our LTspice model of the diode and extracting the value from the simulation. The estimated peak power efficiency, defined as the ratio between power dissipated in R_L and total power consumption (410 nW without considering bias resistors) after the start-up time, was about 60% with a $50\ \Omega$ load and a 500 pF smoothing capacitor.

Conclusions

We have successfully demonstrated a superconducting circuit based on vortex diodes, showing correct full-wave rectification and characterizing the device margins. As a proof-of-concept, we achieved efficient AC-to-DC conversion by shunting the resistive load with a surface-mount smoothing capacitor to obtain a low-pass filter. However, integrated capacitors would increase the footprint of the device which is undesirable. Instead, in future work the filter could be designed using inductors rather than capacitors, exploiting the high kinetic inductance of superconducting nanowires.

In the supplementary material, we explored using an AC-to-DC converter with an inductor-based filter to create a bias distribution network for SNSPDs. In our analysis, we had to assume that the diodes were optimized to operate at 50 MHz and higher frequencies in continuous mode with ideal margins (and thus this design is conditional on significant future advancement of the work demonstrated experimentally so far). Nonetheless, the design

demonstrates the relevance and future potential of superconducting diodes in any cryogenic system that requires dynamically tunable DC bias currents.

For a NbN micro-bridge with these dimensions, our model suggests that the maximum frequency should be much higher than 3 MHz or even 20 MHz: relaxation oscillations in NbN superconducting nanowires have been observed up to 1.25 GHz.⁴¹ Thus, it may be possible to optimize geometry, material properties of the diode, and the load on the device to minimize the hotspot growth and heat dissipation and reach higher frequencies (e.g. by changing substrate to improve thermal transfer). Moreover, new circuit topologies might be introduced to enlarge the operating margins, and thus the tunability range for the output current.

Improving the rectification efficiency will benefit margins, speed, and device footprint. In particular, a symmetric rectifier geometry with large margins would be achievable with $\eta \gg 33\%$. Following our results and the literature,³³ it might be possible to further improve η by decreasing the thickness to 5 nm or less (typical for SNSPDs). We fabricated only wires with a 1 μm width (smaller than the Pearl length), but using wider wires might also increase the efficiency. In a wider micro-bridge under the same applied magnetic field, higher Meissner currents are generated and thus the asymmetric effect might increase. Moreover, if the width exceeds the Pearl length of the film, the current flows along the edges, and thus closer to the defect which might further improve the efficiency of the diode.

For future designs of large-scale diode circuits, the need for an external magnetic field uniformly applied across the chip will limit the integration with field-sensitive superconducting devices. Therefore, vortex diodes based on NbN could be integrated with ferromagnetic thin films to localize the field and enhance the rectification efficiency, similar to the approach by Hou et al.³⁶

The results of this work can be seen as a fundamental starting point for future development in the field of integrated power electronics based on superconducting diodes in thin film platforms.

Note added: During the submission process of this work we became aware of a related work on superconducting rectifiers.⁴²

Methods

Fabrication process

All the tested devices were fabricated with the same process: we deposited the NbN films on 300 nm thick silicon oxide on silicon substrates in an AJA sputtering system; then, we patterned the devices with electron-beam lithography, using a positive-tone resist (ZEP530A) with cold development in *o*-Xylene, and CF₄ reactive ion etching (RIE).⁶

Measurement setup for I-V curves and half-wave rectification

We performed the measurements in a liquid helium dewar at 4.2 K. The chip was glued to a PCB and the pads of the devices were connected to the pins through aluminum wire bonds. The PCB was then placed in a custom cryogenic probe with 28 spring-loaded RF sub-miniature push-on connectors.⁴³ The out-of-plane magnetic field was applied with a superconducting solenoid mounted on the cryogenic probe in close proximity to the chip. The solenoid was controlled by a DC current source.

For each point of the curves in figure 2a and figure 3b, a DC current was applied with a low-noise battery (SRS SIM928) in series with a 10 k Ω resistor, and the voltage across the device was measured by a multi-meter (Keithley 2001) in series with a 1 M Ω resistor.

In figure 2b, the critical currents for each point were found by averaging over 500 I-V curves, which were obtained by applying a 1 kHz triangular waveform with an arbitrary waveform generator (AWG, Agilent AWG33622A). A 10 k Ω bias resistor was used and the voltage across the diode was measured with a 2 GHz real-time oscilloscope (LeCroy 620Zi) with 1 M Ω input impedance. Half-wave rectification was obtained using the same setup and averaging over 100 traces (see supplementary material). For figure 2c, we used the same

configuration but the impedance of the oscilloscope was set to $50\ \Omega$ and the biasing signal was a sinusoidal wave. Each point of the curve is the average of 1000 values.

Measurement setup for full-wave rectification

We performed the measurements in a liquid helium dewar at 4.2 K, as described in the previous section. For all the full-wave rectification tests, the input current i_{IN} was provided with a differential setup: the signal was sent to the IN+ terminal by the AWG in series with a $5\ \text{k}\Omega$ surface-mount resistor placed on the PCB at 4.2 K; simultaneously, the inverted signal was sent to IN- using the same configuration. The two input lines were $50\ \Omega$ matched thanks to a surface-mount $50\ \Omega$ resistor to ground in front of the bias resistors. A $100\ \Omega$ load resistor was placed on the PCB at 4.2 K, and wire bonded to the OUT- and OUT+ terminals of the rectifier. The output current i_{OUT} was calculated by measuring the voltage across the load resistor $V(\text{OUT+}) - V(\text{OUT-})$ with a differential readout: for figure 1d, 3c, 3d, and 4b, both the nodes were connected to the $50\ \Omega$ input ports of the scope; for figure 4a, both output voltages were filtered by a bias tee, attenuated by 10 dB, and amplified by two low-noise amplifiers in series (RF Bay LNA-2500, bandwidth: 10 kHz to 2500 MHz, gain: 25 dB, and RF Bay LNA-2000, bandwidth: 10 kHz to 2000 MHz, gain: 26 dB). In both configurations, the total load resistance R_{L} was calculated considering the $100\ \Omega$ resistor in parallel with the $100\ \Omega$ differential resistance of the scope (or amplifiers). A more detailed circuit schematic of the differential measurement setup is shown in the supplementary material. For all the figures, the shown waveforms were obtained by averaging multiple traces.

In figure 3c, at each tested frequency, we swept the input current amplitude from $100\ \mu\text{A}$ to $300\ \mu\text{A}$ with an increment of $0.2\ \mu\text{A}$ and observed if full-wave rectification was achieved. Data points in the figure are associated with the current amplitude for which there was a transition between correct and incorrect operation.

LTspice modeling

We created the LTspice model of the diode by slightly modifying the existing hotspot-growth model of a superconducting nanowire.⁴⁰ We kept the same material parameters, modified the thickness and width, and introduced a critical current that depends on the current flow direction. We did not model the hotspot growth in the real geometry of the device. Instead, we considered the diode as a 7.5-squares long wire with a constant width equal to the constriction width (400 nm). For simulating the bridge rectifier, we extracted the number of squares for each branch from the device geometry (15 for the left branch and 150 for the right branch) to estimate L_R and L_L (the sheet inductance was set to 30 pH/sq). For the left branch, L_L was reproduced by the inductances included in the models of D_2 and D_3 . For the right branch, two lumped inductors were added in series with D_1 and D_4 to reach the value of L_R .

We successfully modeled the time-domain behavior of the bridge rectifier shown in figure 1d by setting the high critical current and η to the maximum values obtained in figure 3c for the 13 nm thick film (261 μ A and 40% respectively). The comparison between the model and experimental data is shown in the supplementary material. The simulated rectifier did not have the same limitations in frequency and margins as the experiment because the rectification factor was set to be constant, and substrate temperature changes caused by self-heating effects, which might alter the hotspot reset time, were not considered. Nevertheless, the model was accurate enough to estimate the power efficiency of the bridge rectifier, considering that the power dissipation mainly depends on the modeled electrothermal behavior of the wires. We estimated the power efficiency of the AC-to-DC converter by setting the rectification factor of the model to 18% to match the value of DC current obtained in the experiment and the high critical current to 261 μ A. In the supplementary material, we show the comparison between experimental and simulated output current at 50 MHz in burst mode. The peak power efficiency was calculated after the start-up time when the output current saturated.

Acknowledgements

This material is based upon work supported by the U.S. Department of Energy, Office of Science, Office of Basic Energy Sciences, under Award Number DE-AC02-07CH11359. O.M. acknowledges support from the NDSEG Fellowship program. A.B. acknowledges support from Politecnico di Torino. R.A.F. acknowledges support from the DOE under the National Laboratory LAB 21-2491 Microelectronics grant. M.Colangelo acknowledges support from MIT Claude E. Shannon award. The data that support the findings of this study are available from the corresponding author upon reasonable request. The authors have no conflicts of interest to report. The authors would like to thank Prof. Christoph Strunk and Prof. Philip Moll for advising in the interpretation of the results.

Contributions

M.Castellani conceived the idea, fabricated the devices, supervised the experiment, analysed the data, and performed the simulations. A.B. and O.M contributed to the design of the diode geometry. A.B. O.M and R.A.F assisted in the measurement. All the authors contributed to the discussions and production of the manuscript.

References

- (1) Alexander, K. et al. A manufacturable platform for photonic quantum computing. 2024; ArXiv: 2404.17570.
- (2) Grünenfelder, F.; Boaron, A.; Resta, G. V.; Perrenoud, M.; Rusca, D.; Barreiro, C.; Houlmann, R.; Sax, R.; Stasi, L.; El-Khoury, S.; Hänggi, E.; Bosshard, N.; Bussièeres, F.; Zbinden, H. Fast single-photon detectors and real-time key distillation enable high secret-key-rate quantum key distribution systems. *Nature Photonics* **2023**, *17*, 422–426.

- (3) Khan, S.; Primavera, B. A.; Chiles, J.; McCaughan, A. N.; Buckley, S. M.; Tait, A. N.; Lita, A.; Biesecker, J.; Fox, A.; Olaya, D.; Mirin, R. P.; Nam, S. W.; Shainline, J. M. Superconducting optoelectronic single-photon synapses. *Nature Electronics* **2022**, *5*, 650–659.
- (4) Lee, S.; Polakovic, T.; Armstrong, W.; Dibos, A.; Draher, T.; Pastika, N.; Meziani, Z.-E.; Novosad, V. Beam Tests of SNSPDs with 120 GeV Protons. 2024; _eprint: 2312.13405.
- (5) Oripov, B. G.; Rampini, D. S.; Allmaras, J.; Shaw, M. D.; Nam, S. W.; Korzh, B.; McCaughan, A. N. A superconducting nanowire single-photon camera with 400,000 pixels. *Nature* **2023**, *622*, 730–734.
- (6) Castellani, M.; Medeiros, O.; Foster, R. A.; Buzzi, A.; Colangelo, M.; Bienfang, J. C.; Restelli, A.; Berggren, K. K. A Nanocryotron Ripple Counter Integrated with a Superconducting Nanowire Single-Photon Detector for Megapixel Arrays. *arXiv preprint arXiv:2304.11700* **2023**,
- (7) Huang, Y.-H.; Zhao, Q.-Y.; Hao, H.; Liu, N.-T.; Liu, Z.; Deng, J.; Yang, F.; Ru, S.-Y.; Tu, X.-C.; Zhang, L.-B.; Jia, X.-Q.; Chen, J.; Kang, L.; Wu, P.-H. Monolithic integrated superconducting nanowire digital encoder. *Applied Physics Letters* **2024**, *124*, 192601, _eprint: https://pubs.aip.org/aip/apl/article-pdf/doi/10.1063/5.0202827/19961586/192601_1_5.0202827.pdf.
- (8) Miyajima, S.; Yabuno, M.; Miki, S.; Yamashita, T.; Terai, H. High-time-resolved 64-channel single-flux quantum-based address encoder integrated with a multi-pixel superconducting nanowire single-photon detector. *Opt. Express* **2018**, *26*, 29045–29054, Publisher: Optica Publishing Group.
- (9) Yabuno, M.; Miyajima, S.; Miki, S.; Terai, H. Scalable implementation of a supercon-

- ducting nanowire single-photon detector array with a superconducting digital signal processor. *Opt. Express* **2020**, *28*, 12047–12057, Publisher: Optica Publishing Group.
- (10) Viskova, T. Cryo-CMOS ICs for Scalable Superconducting Nanowire Single Photon Detectors. 2022.
- (11) Acharya, R. et al. Multiplexed superconducting qubit control at millikelvin temperatures with a low-power cryo-CMOS multiplexer. *Nature Electronics* **2023**, *6*, 900–909.
- (12) Niu, J. et al. Low-loss interconnects for modular superconducting quantum processors. *Nature Electronics* **2023**, *6*, 235–241.
- (13) Nadeem, M.; Fuhrer, M. S.; Wang, X. The superconducting diode effect. *Nature Reviews Physics* **2023**, *5*, 558–577.
- (14) Ando, F.; Miyasaka, Y.; Li, T.; Ishizuka, J.; Arakawa, T.; Shiota, Y.; Moriyama, T.; Yanase, Y.; Ono, T. Observation of superconducting diode effect. *Nature* **2020**, *584*, 373–376, Publisher: Nature Publishing Group.
- (15) Bauriedl, L.; Bäuml, C.; Fuchs, L.; Baumgartner, C.; Paulik, N.; Bauer, J. M.; Lin, K.-Q.; Lupton, J. M.; Taniguchi, T.; Watanabe, K.; others Supercurrent diode effect and magnetochiral anisotropy in few-layer NbSe₂. *Nature communications* **2022**, *13*, 1–7, Publisher: Nature Publishing Group.
- (16) Paolucci, F.; De Simoni, G.; Giazotto, F. A gate- and flux-controlled supercurrent diode effect. *Applied Physics Letters* **2023**, *122*, 042601, eprint: <https://doi.org/10.1063/5.0136709>.
- (17) Golod, T.; Krasnov, V. M. Demonstration of a superconducting diode-with-memory, operational at zero magnetic field with switchable nonreciprocity. *Nature Communications* **2022**, *13*, 3658.

- (18) Pal, B.; Chakraborty, A.; Sivakumar, P. K.; Davydova, M.; Gopi, A. K.; Pandeya, A. K.; Krieger, J. A.; Zhang, Y.; Ju, S.; Yuan, N.; others Josephson diode effect from Cooper pair momentum in a topological semimetal. *Nature Physics* **2022**, *18*, 1228–1233, Publisher: Nature Publishing Group.
- (19) Wu, H.; Wang, Y.; Xu, Y.; Sivakumar, P. K.; Pasco, C.; Filippozzi, U.; Parkin, S. S.; Zeng, Y.-J.; McQueen, T.; Ali, M. N. The field-free Josephson diode in a van der Waals heterostructure. *Nature* **2022**, *604*, 653–656, Publisher: Nature Publishing Group.
- (20) Narita, H.; Ishizuka, J.; Kawarazaki, R.; Kan, D.; Shiota, Y.; Moriyama, T.; Shimakawa, Y.; Ognev, A. V.; Samardak, A. S.; Yanase, Y.; others Field-free superconducting diode effect in noncentrosymmetric superconductor/ferromagnet multilayers. *arXiv preprint arXiv:2206.00483* **2022**,
- (21) Chahid, S.; Teknowijoyo, S.; Mowgood, I.; Gulian, A. High-frequency diode effect in superconducting Nb₃Sn micro-bridges. 2022; <https://arxiv.org/abs/2211.11537>.
- (22) Bean, C. P.; Livingston, J. D. Surface Barrier in Type-II Superconductors. *Phys. Rev. Lett.* **1964**, *12*, 14–16, Publisher: American Physical Society.
- (23) Korzh, B. et al. Demonstration of sub-3 ps temporal resolution with a superconducting nanowire single-photon detector. *Nature Photonics* **2020**, *14*, 250–255.
- (24) McCaughan, A. N.; Abebe, N. S.; Zhao, Q.-Y.; Berggren, K. K. Using Geometry To Sense Current. *Nano Letters* **2016**, *16*, 7626–7631, Publisher: American Chemical Society.
- (25) Butters, B. A.; Baghdadi, R.; Onen, M.; Toomey, E. A.; Medeiros, O.; Berggren, K. K. A scalable superconducting nanowire memory cell and preliminary array test. *Superconductor Science and Technology* **2021**, *34*, 035003, Publisher: IOP Publishing.

- (26) Buzzi, A.; Castellani, M.; Foster, R. A.; Medeiros, O.; Colangelo, M.; Berggren, K. K. A nanocryotron memory and logic family. *Applied Physics Letters* **2023**, *122*, 142601.
- (27) Foster, R. A.; Castellani, M.; Buzzi, A.; Medeiros, O.; Colangelo, M.; Berggren, K. K. A superconducting nanowire binary shift register. *Applied Physics Letters* **2023**, *122*, 152601.
- (28) Colangelo, M.; Zhu, D.; Santavicca, D. F.; Butters, B. A.; Bienfang, J. C.; Berggren, K. K. Compact and Tunable Forward Coupler Based on High-Impedance Superconducting Nanowires. *Phys. Rev. Appl.* **2021**, *15*, 024064, Publisher: American Physical Society.
- (29) Wagner, A.; Ranzani, L.; Ribeill, G.; Ohki, T. A. Demonstration of a superconducting nanowire microwave switch. *Applied Physics Letters* **2019**, *115*, 172602.
- (30) Toomey, E.; Segall, K.; Castellani, M.; Colangelo, M.; Lynch, N.; Berggren, K. K. Superconducting Nanowire Spiking Element for Neural Networks. *Nano Letters* **2020**, *20*, 8059–8066, Publisher: American Chemical Society.
- (31) Lombo, A. E.; Lares, J.; Castellani, M.; Chou, C.-N.; Lynch, N.; Berggren, K. K. A superconducting nanowire-based architecture for neuromorphic computing. *Neuromorphic Computing and Engineering* **2022**, *2*, 034011, Publisher: IOP Publishing.
- (32) Zhao, Q.-Y.; McCaughan, A. N.; Dane, A. E.; Berggren, K. K.; Ortlepp, T. A nanocryotron comparator can connect single-flux-quantum circuits to conventional electronics. *Superconductor Science and Technology* **2017**, *30*, 044002, Publisher: IOP Publishing.
- (33) Vodolazov, D. Y.; Peeters, F. M. Superconducting rectifier based on the asymmetric surface barrier effect. *Phys. Rev. B* **2005**, *72*, 172508, Publisher: American Physical Society.

- (34) Cerbu, D.; Gladilin, V. N.; Cuppens, J.; Fritzsche, J.; Tempere, J.; Devreese, J. T.; Moshchalkov, V. V.; Silhanek, A. V.; Vondel, J. V. d. Vortex ratchet induced by controlled edge roughness. *New Journal of Physics* **2013**, *15*, 063022, Publisher: IOP Publishing.
- (35) Semenov, A.; Charaev, I.; Lusche, R.; Ilin, K.; Siegel, M.; Hübers, H.-W.; Braloviifmmode \acuteec\else é\fi, N.; Dopf, K.; Vodolazov, D. Y. Asymmetry in the effect of magnetic field on photon detection and dark counts in bended nanostrips. *Phys. Rev. B* **2015**, *92*, 174518, Publisher: American Physical Society.
- (36) Hou, Y.; Nichele, F.; Chi, H.; Lodesani, A.; Wu, Y.; Ritter, M. F.; Haxell, D. Z.; Davydova, M.; Ilić, S.; Bergeret, F. S.; others Ubiquitous Superconducting Diode Effect in Superconductor Thin Films. *arXiv preprint arXiv:2205.09276* **2022**,
- (37) Zhang, X.; Huan, Q.; Ma, R.; Zhang, X.; Huang, J.; Liu, X.; Peng, W.; Li, H.; Wang, Z.; Xie, X.; You, L. Superconducting Diode Effect in a Constricted Nanowire. *Advanced Quantum Technologies* *n/a*, 2300378, eprint: <https://onlinelibrary.wiley.com/doi/pdf/10.1002/qute.202300378>.
- (38) Suri, D.; Kamra, A.; Meier, T. N. G.; Kronseder, M.; Belzig, W.; Back, C. H.; Strunk, C. Non-reciprocity of vortex-limited critical current in conventional superconducting micro-bridges. *Applied Physics Letters* **2022**, *121*, 102601, eprint: <https://doi.org/10.1063/5.0109753>.
- (39) Hortensius, H. L.; Driessen, E. F. C.; Klapwijk, T. M.; Berggren, K. K.; Clem, J. R. Critical-current reduction in thin superconducting wires due to current crowding. *Applied Physics Letters* **2012**, *100*, 182602.
- (40) Berggren, K. K.; Zhao, Q.-Y.; Abebe, N.; Chen, M.; Ravindran, P.; McCaughan, A.; Bardin, J. C. A superconducting nanowire can be modeled by using SPICE. *Superconductor Science and Technology* **2018**, *31*, 055010, Publisher: IOP Publishing.

- (41) Castellani, M. Design of Superconducting Nanowire-Based Neurons and Synapses for Power-Efficient Spiking Neural Networks. M.Sc. thesis, Politecnico di Torino, 2020.
- (42) Ingra-Aynés, J.; Hou, Y.; Wang, S.; Chu, E.-D.; Mukhanov, O. A.; Wei, P.; Moodera, J. S. Highly Efficient Superconducting Diodes and Rectifiers for Quantum Circuitry. 2024.
- (43) Butters, B. A. Digital and Microwave Superconducting Electronics and Experimental Apparatus. PhD Thesis, Massachusetts Institute of Technology, 2022.

Supplementary Material

A superconducting full-wave bridge rectifier

Matteo Castellani, Owen Medeiros, Alessandro Buzzi, Reed A. Foster, Marco Colangelo, and Karl K. Berggren*

*Electrical Engineering and Computer Science, Massachusetts Institute of Technology,
Cambridge, MA, USA*

E-mail: mcaste@mit.edu

Half-wave rectification

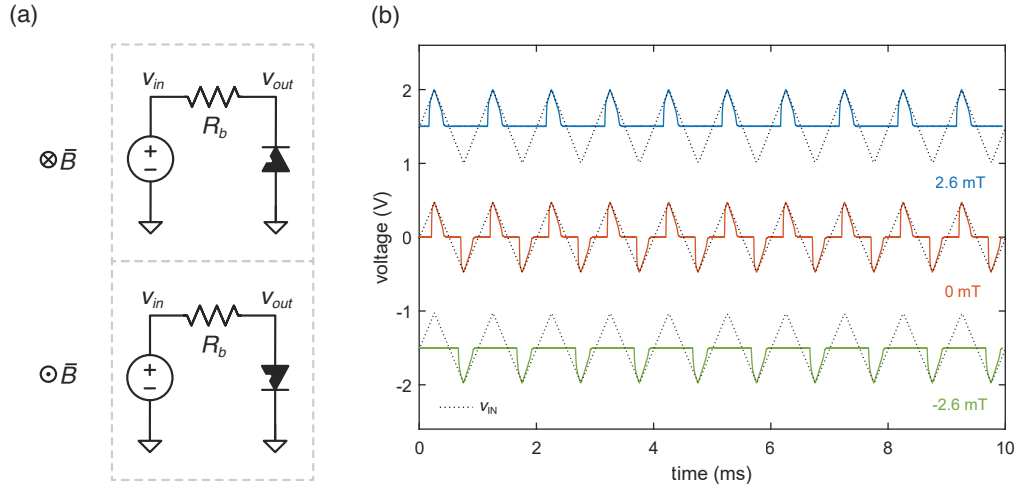


Figure S1: Half-wave rectification of a triangular wave. (a) Circuit schematic of a current-biased superconducting diode for opposite diode polarities. This setup was used both to measure I-V curves and to demonstrate half-wave rectification ($R_b = 10 \text{ k}\Omega$). (b) Half-wave rectification of a 1 kHz triangular wave for zero, positive, and negative magnetic fields. The triangular waves in dashed lines (v_{IN}) are theoretical input signals scaled to have the same amplitude of v_{OUT} . Traces are vertically shifted for clarity. Each trace is the average of 100 different traces acquired in sequence, to increase the signal-to-noise-ratio.

A typical use for a single superconducting diode is half-wave rectification of a periodic signal. Using the same setup as in the I-V curve measurement (a simplified schematic is shown in figure S1a), we confirmed half-wave rectification of a triangular wave at 1 kHz, shown in figure S1b. The maximum current was set to a value in between the critical current of the wire with zero field, and I_c^- (I_c^+ for negative magnetic field). With zero applied field, a resistive state was generated on both the positive and negative amplitudes of the curve. For positive magnetic fields, only positive currents generated a voltage on the output. An analogous and opposite effect was observed for negative fields. We did not test the maximum operating frequency of the diode performing half-wave rectification.

Bridge rectifier with an asymmetric geometry

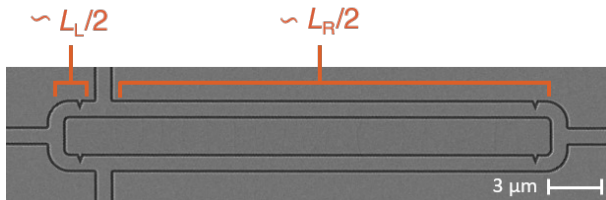


Figure S2: Scanning electron micrograph of the bridge rectifier with an asymmetric geometry. The red labels indicate the section of the wire in the superconducting loop associated with the kinetic inductances L_R and L_L . The ratio L_R/L_L is 10.

Figure S2 shows the scanning electron micrograph of the bridge rectifier we used to obtain most of the results of this work. The ratio L_R/L_L is 10.

Measurement setup for full-wave rectification

Figure S3 shows the circuit schematic of the differential measurement setup described in the Methods section (without amplifiers). We used the oscilloscope to acquire both the input and output signals. The input current waveforms showed in the results were extracted by subtracting the two input signals (v_{IN} and $-v_{IN}$) and dividing by $2R_b$. The output currents

were extracted by subtracting the two output voltages and dividing them by the equivalent parallel resistance (R_L) of R_{L0} and the $100\ \Omega$ differential resistance of the scope.

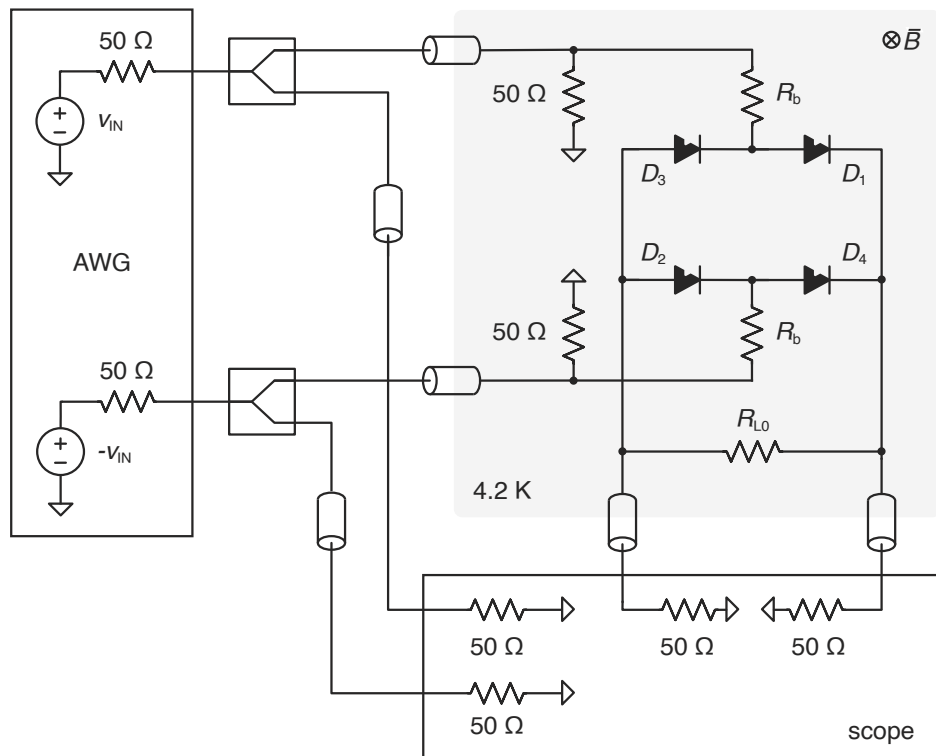


Figure S3: Circuit schematic of the measurement setup for full-wave rectification. An AWG generates two identical but inverted signals (v_{IN} and $-v_{IN}$) that are sent to two splitters. For each splitter, one port is connected to the scope and the other port is connected to a bias surface-mount resistor R_b and a parallel surface-mount $50\ \Omega$ resistor (this resistor ensures impedance matching between AWG and device), to drive one of the two input ports of the rectifier. A surface-mount resistor R_{L0} , connects the two output ports of the rectifier. The output voltage across R_{L0} is differentially measured by the oscilloscope. All the components in the gray box are at 4.2K. The magnetic field is applied to all the devices at low temperature. Coaxial cables connects the circuit to room-temperature electronics.

Full-wave rectification: experiment and simulation

Figure S4 shows the comparison between the experimental and simulated full-wave rectification of a continuous sinusoidal signal at 3 MHz. The simulation was performed on the bridge rectifier with $L_R/L_L = 10$, using the LTspice model described in the Methods section.

In the simulated output, the fast rising edge, which corresponds to the switch of two

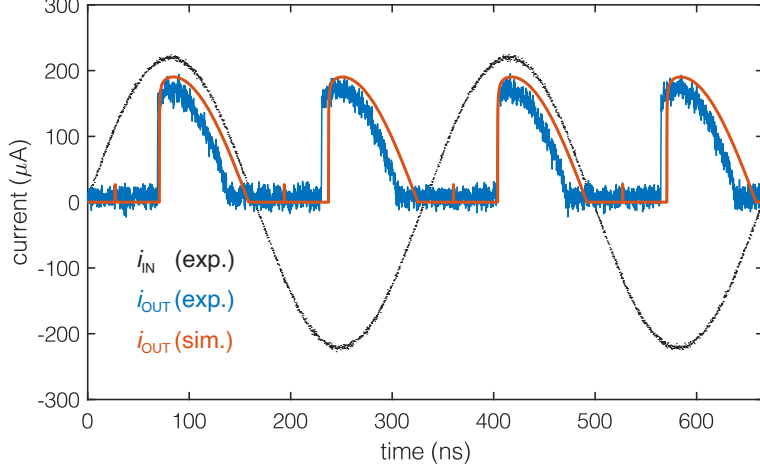


Figure S4: Comparison between experimental and simulated full-wave rectification at 3 MHz. The black trace is the experimental input current of the rectifier. The blue trace is the experimental output current without averaging. The red trace is the output current simulated with the parameters listed in the Methods section.

diodes in the rectifier, always happens at the same time for each semi-period. In the experimental trace, the switch happens at different times for each semi-period, due to noise and thermal fluctuations in the devices.

In the experiment, the peak output current is slightly lower than in simulations. Moreover, the experimental output signal drops to zero for a lower input current than in simulations. This difference might be explained by the retrapping current of the diode being higher than in the LTspice model.

In the simulation, there is a short pulse of about $30 \mu\text{A}$ at each semi-period before the large pulse (about $180 \mu\text{A}$). This is a consequence of the following behavior: when the positive input current is rising, D_3 switches before D_4 and the current does not increase fast enough to sustain a stable hotspot in D_3 ; therefore, D_3 quickly resets (a short pulse is generated on the output), and current still flows through it; as a consequence, the current needs to further increase until a stable hotspot in both D_3 and D_4 is created (large switch in the plot). Considering that the simulation mimicked the experimental result, this behavior might explain the reduced margins for full-wave rectification: the lower current limit of the experimental margins ($218 \mu\text{A}$ at 100 Hz) was higher than expected. However, the effect

should equally modify the margins also in the experimental I-V curves but we did not observe it. Therefore, further characterization of the circuit is required to fully understand this problem. In simulations, the effect disappears at higher frequencies (e.g. at 50 MHz) because the input current increases fast enough to sustain a hotspot when D_2 or D_3 switch.

AC-to-DC conversion: experiment and simulation

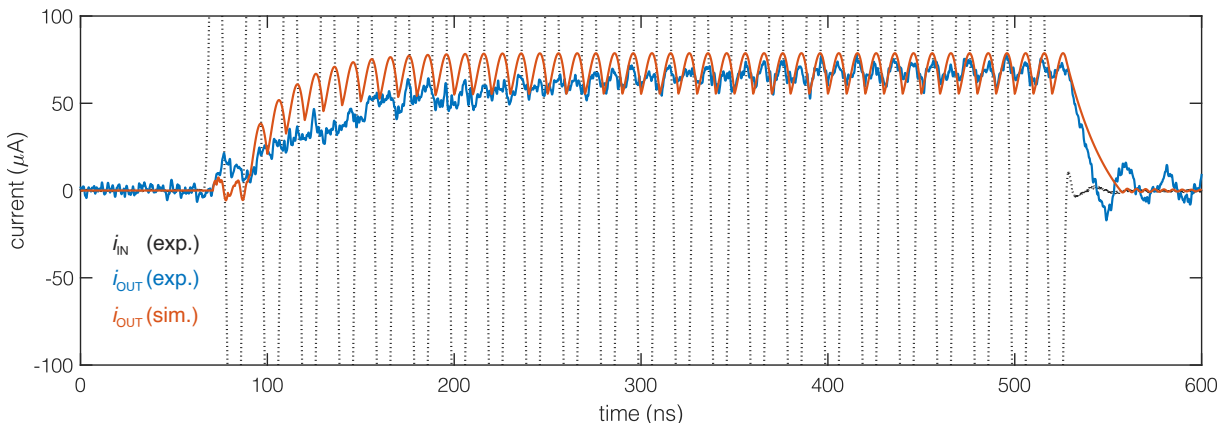


Figure S5: Comparison between experimental and simulated time-domain behavior of the AC-to-DC converter. The black dashed trace is the input current (the top and bottom portions of the signals are not shown to focus on the output trace). The blue trace is the experimental output current through the load resistor without averaging. The red trace is the simulated output current.

Figure S5 shows the comparison between the experimental (not averaged) and the simulated output current of the AC-to-DC converter. We did not use an amplifier because its limited bandwidth near DC altered the shape of the signal.

During the first several periods of the input signal (for about 300 ns), the rectifier did not operate correctly. In simulations, we observed this behavior when we took into account the inductance of the wire bonds between the PCB and the ports of the rectifier (with values in simulation on the order of 1 nH). The simulated trace in this plot was obtained with zero inductances from the wire bonds.

The simulated ripple amplitude seemed to be lower than in the experiment. Probably the reason is that we did not consider parasitic capacitances in the setup that might have

altered the equivalent C of the filter. For example, the capacitance of the coaxial cables on the output ports, in parallel with C , could have increased the RC time constant of the filter.

For both the experiment and the simulation, there was a ringing transient at the falling edge of the burst. In the experiment, the ringing amplitude was higher due to the ringing behavior of the input signal.

Design and simulation of a bias distribution network

We suggest a circuit design to solve the problem of how to bias a network of superconducting devices on a chip with dynamically tunable DC currents. This design has potential value across a range of problems such as biasing detector arrays, nanocryotron electronics, and neuromorphic systems.^{1,2}

The basic idea is to build integrated AC-to-DC converters to individually and dynamically set the bias level of each of an array of devices (e.g. SNSPDs). Doing this with DC cables would be challenging, however setting the DC bias levels through rectified AC signals that are frequency multiplexed on a single RF line would help decrease the number of cables coming out of the cryostat. Indeed, a similar frequency-multiplexed biasing and readout system has already been proposed for SNSPDs.³ In this proposal, the sensors were directly biased with AC signals, thus the photon detection efficiency was time-dependent.⁴ Exploiting the advantages of frequency multiplexing while maintaining a DC bias, and thus not sacrificing efficiency, would be optimal. This goal can be achieved by using integrated AC-to-DC converters to rectify the AC signals at low temperatures. The converters can be designed using superconducting bridge rectifiers.

In this circuit, each cryogenic device is biased by an AC-to-DC converter. Each converter is coupled to a superconducting resonator with a unique resonant frequency, and all the resonators are coupled to a single RF line coming out of the cryostat. The current value of each bias line is thus frequency multiplexed. With the current performance of the bridge

rectifier, the maximum frequency to sustain full-wave rectification is 3 MHz. With this and lower frequency values, the footprint of the resonators would be too large. Moreover, the margins would be too small to allow fine tuning. Therefore, for this design, we assumed the devices had been already optimized to operate in a range of frequencies between 50 MHz and 150 MHz with sufficiently large margins.

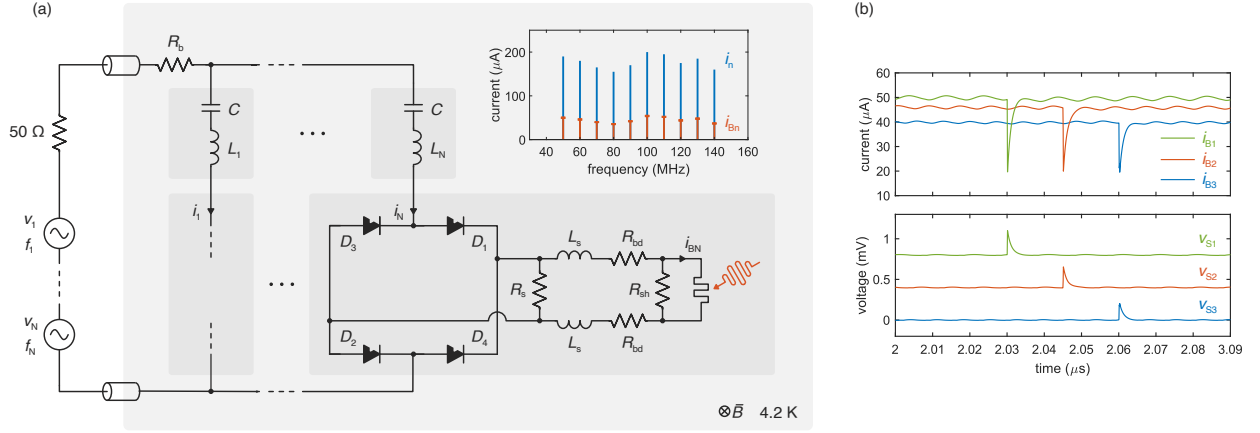


Figure S6: Design and simulation of a bias distribution network based on superconducting bridge rectifiers. (a) Circuit schematic of a network to bias N SNSPDs. All the components in the gray box are placed at 4.2 K, and the field is applied to the entire system. The voltage source at room temperature generates N sinusoidal signals (v_n) at N different frequencies (f_n). Each signal couples to a specific superconducting LC series resonator (C and L_n). The resonators are connected in parallel. Each resonator is in series with a bridge rectifier, which drives an inductive low-pass filter. The filter generates a DC current passing through a shunted SNSPD. The upper-right inset shows the distribution of different bias levels for $N = 10$. The amplitude of the AC input current i_n of each rectifier is in blue. The DC current through the SNSPD, with associated ripple (error bars), is in red. (b) Simulated time-domain behavior for three SNSPDs (respectively coupled to signals at 50 MHz, 60 MHz, 70 MHz) switching at different times in the network of ten SNSPDs. Upper panel: current through the SNSPDs. lower panel: voltage v_{Sn} across the shunt resistor R_{sh} of the SNSPDs. Traces in the lower panel are vertically shifted for clarity. Circuit parameters: $I_c^+ = 100 \mu\text{A}$, $I_c^- = 200 \mu\text{A}$, $R_b = 45 \Omega$, $C = 1 \text{ pF}$, $R_s = 5 \Omega$, $L_s = 250 \text{ nH}$, $R_{sh} = 10 \Omega$, $R_{bd} = 2.5 \Omega$, SNSPD inductance: $L_d = 10 \text{ nH}$.

Figure S6a shows the circuit schematic of the proposed architecture for SNSPD biasing. A single RF line is used to send N frequency components to the associated N series lumped LC resonators, which are connected in parallel to each other (LC circuits might be replaced by CPW resonators as in the work of Doerner et al.³). The capacitance C is constant for

all the resonators, L_n varies. In series with each resonator, there is an AC-to-DC converter that biases a single SNSPD. For each frequency component of the input signal, only one branch is at resonance, and thus ideally, the AC signal is delivered to only one converter. The converter is composed of a bridge rectifier and an inductive low-pass filter made with L_s , R_s and R_L . We opted for this solution because superconducting nanowire-based kinetic inductances have much lower footprints than integrated capacitors. The SNSPD is in series with R_L and shunted by R_{sh} . The system is fully differential and the values of R_b and R_s are chosen so that their sum is 50Ω to ensure impedance matching with the room-temperature voltage generator at each frequency.

For this architecture, we chose to bias SNSPDs as example devices but the scheme can be used for other superconducting devices. It is worth using this structure for SNSPDs only if additional superconducting circuitry is added to read out the detector's outputs and eventually frequency multiplex them, such that there is only one readout line. A possible solution might be to use a single RF line for both frequency-multiplexed biasing and readout, similar to Doerner et al.³ To do so the low-pass filter should be redesigned such that the impedance seen by the input voltage source drastically increases after a detection event and the impedance change can be measured on the input port. Another readout solution can be to thermally couple the detectors or their shunt resistors to a common superconducting line, similar to the configuration of Oripov et al.⁵ Each section of the common line coupled to a different detector could be shunted with a different value of resistance so that the output would be amplitude-multiplexed, as proposed by Gaggero et al.⁶ As a third solution, SNSPDs could directly drive nanocryotron electronics that perform signal processing at low temperatures, removing the need to acquire the detector's output with room-temperature equipment.

We simulated the system of figure S6, without considering readout architectures, in LTspice by using the model of the rectifier with a constant 33% rectification efficiency, $L_L = 200\text{ pH}$, and $L_R = 2\text{ nH}$. The inset in figure S6a shows the different levels of input

current of the bridge rectifier set by the N components of the voltage source (blue bars), and the associated DC output currents (red bars), for $N = 10$. The values of input currents were chosen arbitrarily inside the input margins. The DC currents follow the distribution profile of the input signals because the bias levels of the 10 devices can be individually controlled. The range of possible bias levels goes from $35.5 \mu\text{A}$ to $54 \mu\text{A}$.

Figure S6b shows the simulation result of 3 out of the 10 SNSPDs detecting photons at different times. The detectors are biased with three different values of current that are set by the voltage sources. After the detection events, the bias current is reset to the initial value and the detectors are ready to fire again. The switching event of one of the detectors does not alter the operation of the other devices.

The system reaches a steady state with stable DC currents after about $1 \mu\text{s}$ (start-up time) from when the input voltage source is turned on. After this time, the value of one of the bias currents can be updated from the highest to the lowest level of the margins in about 200 ns . During the update the current alteration of the other channel is negligible.

In the simulated circuit, the 10 channels are separated in frequency by $\Delta f = 10 \text{ MHz}$. To scale up the system (increasing N), Δf will need to be lowered if the range of allowed frequencies is fixed (assuming that the rectifier operates only between 50 MHz and 150 MHz with reasonably small footprints). However, decreasing Δf increases the cross-talk between resonators and thus the effective ripple of the DC currents. If the ripple amplitude becomes comparable with the current margins of the rectifier, fine-tuning the currents is no longer possible. With the parameters used, this condition is reached for $\Delta f < 6.5 \text{ MHz}$. With $\Delta f = 6.5 \text{ MHz}$ the largest ripple is about 15% of the total margin. With $\Delta f = 10 \text{ MHz}$ the larger ripple is about 9.5% of the total margin. Considering these results, and considering that the rectifier can operate up to 150 MHz , the current design will not allow more than 15 channels.

We estimated the power consumption of this system in simulations. The average consumption at low temperatures is 810 nW per device, without switching events of the biased

devices. 92% of this power is dissipated by R_b , 7% of the power is dissipated by the bridge rectifier and the filter, and 1% is dissipated by the R_{bd} bias resistors.

The designed architecture would have a relatively large footprint when implemented. The area of each module would be dominated by the capacitor C and the inductor L_n . If rectifiers operating at higher frequencies were demonstrated, the footprint of the resonators could be decreased. Otherwise, a multi-layer fabrication process might be used to minimize the occupied area. In particular, parallel-plate capacitors could be used. Moreover, a normal metal layer should be included for the integrated resistors.

Another circuit element that largely contributes to the occupied area is the large inductor in the low-pass filter. Its inductance can be in principle reduced, however, the ripple on the output current would increase.

References

- (1) Castellani, M. Design of Superconducting Nanowire-Based Neurons and Synapses for Power-Efficient Spiking Neural Networks. M.Sc. thesis, Politecnico di Torino, 2020.
- (2) Lombo, A. E.; Lares, J.; Castellani, M.; Chou, C.-N.; Lynch, N.; Berggren, K. K. A superconducting nanowire-based architecture for neuromorphic computing. *Neuromorphic Computing and Engineering* **2022**, *2*, 034011, Publisher: IOP Publishing.
- (3) Doerner, S.; Kuzmin, A.; Wuensch, S.; Charaev, I.; Boes, F.; Zwick, T.; Siegel, M. Frequency-multiplexed bias and readout of a 16-pixel superconducting nanowire single-photon detector array. *Applied Physics Letters* **2017**, *111*, 032603.
- (4) Doerner, S.; Kuzmin, A.; Wuensch, S.; Siegel, M. Comparison of SNSPDs Biased With Microwave and Direct Currents. *IEEE Transactions on Applied Superconductivity* **2019**, *29*, 1–4.
- (5) Oripov, B. G.; Rampini, D. S.; Allmaras, J.; Shaw, M. D.; Nam, S. W.; Korzh, B.; Mc-

Caughan, A. N. A superconducting nanowire single-photon camera with 400,000 pixels. *Nature* **2023**, *622*, 730–734.

- (6) Gaggero, A.; Martini, F.; Mattioli, F.; Chiarello, F.; Cernansky, R.; Politi, A.; Leoni, R. Amplitude-multiplexed readout of single photon detectors based on superconducting nanowires. *Optica* **2019**, *6*, 823–828, Publisher: Optica Publishing Group.